



## Mechanical Control of Morphogenesis by Fat/Dachsous/Four-Jointed Planar Cell Polarity Pathway

Floris Bosveld *et al.*

*Science* **336**, 724 (2012);

DOI: 10.1126/science.1221071

*This copy is for your personal, non-commercial use only.*

If you wish to distribute this article to others, you can order high-quality copies for your colleagues, clients, or customers by [clicking here](#).

Permission to republish or repurpose articles or portions of articles can be obtained by following the guidelines [here](#).

**The following resources related to this article are available online at [www.sciencemag.org](http://www.sciencemag.org) (this information is current as of May 23, 2012):**

**Updated information and services**, including high-resolution figures, can be found in the online version of this article at:

<http://www.sciencemag.org/content/336/6082/724.full.html>

**Supporting Online Material** can be found at:

<http://www.sciencemag.org/content/suppl/2012/04/11/science.1221071.DC1.html>

A list of selected additional articles on the Science Web sites **related to this article** can be found at:

<http://www.sciencemag.org/content/336/6082/724.full.html#related>

This article **cites 23 articles**, 9 of which can be accessed free:

<http://www.sciencemag.org/content/336/6082/724.full.html#ref-list-1>

This article has been **cited by** 1 articles hosted by HighWire Press; see:

<http://www.sciencemag.org/content/336/6082/724.full.html#related-urls>

This article appears in the following **subject collections**:

Development

<http://www.sciencemag.org/cgi/collection/development>

diffusion coefficients of the fusion proteins by fitting a three-dimensional diffusion model to recovery profiles (text S6 and figs. S19 to S21). We obtained effective diffusion coefficients of  $0.7 \pm 0.2 \mu\text{m}^2/\text{s}$  for Cyclops-GFP,  $3.2 \pm 0.5 \mu\text{m}^2/\text{s}$  for Squint-GFP,  $11.1 \pm 0.6 \mu\text{m}^2/\text{s}$  for Lefty1-GFP, and  $18.9 \pm 3.0 \mu\text{m}^2/\text{s}$  for Lefty2-GFP (Fig. 4B, figs. S18 to S23, and text S6). Thus, increased protein diffusivities reflect increased ranges, indicating that differential diffusivity is a major contributor to the differences in Nodal and Lefty range.

To test whether the experimentally determined values for diffusivity and clearance accurately predict the measured distribution profiles, we numerically simulated signal secretion from a localized source, diffusion, and clearance (12, 14, 26) in a three-dimensional geometry appropriate for blastula embryos (text S7). Using the measured values for diffusivity and clearance, these simulations yielded distribution profiles similar to the experimentally determined protein distributions (fig. S26) and thus provided independent support for the validity of the experimental approaches.

Our results have two major implications. First, differential diffusivity underlies differences in activator/inhibitor range. The differences in range (Cyclops < Squint < Lefty1 < Lefty2) are reflected in the differences in effective diffusion coefficients (Cyclops < Squint < Lefty1 < Lefty2). There is a similar trend in half-lives, but the differences in diffusivity are much more pronounced than the differences in clearance. During embryogenesis, the sources of Nodal and Lefty overlap, but Nodal signaling is active near the source and is inhibited by Lefty farther away. Our results suggest that the lower mobility of Nodal allows its accumulation close to the site of secretion, whereas the high mobility of Lefty leads to rapid long-range dispersal and prevents accumulation near the source. Thus, the differential diffusivity of Nodal and Lefty signals serves as the biophysical basis for the spatially restricted induction of cell fates during embryogenesis.

Second, the previously described network topology of the Nodal/Lefty system and the biophysical properties of Nodals and Leftys measured here support the activator/inhibitor reaction-diffusion model of morphogenesis: A less diffusive activator (Nodal) induces both its own production and that of a more diffusive inhibitor (Lefty) (3, 4). The Nodal/Lefty reaction-diffusion system is further constrained by pre-patterns and rapid cell fate specification; thus, the system results in graded pathway activation during mesendoderm induction and exclusive pathway activation on the left during left-right specification (see text S2 for detailed discussion). Mathematical models have postulated that the inhibitor in reaction-diffusion systems must have a higher diffusion coefficient than the activator. Several models suggest that clearance-normalized inhibitor and activator diffusion coefficients differ by a factor of at least 6, that is,  $\mathcal{R} = (D/k_1)_{\text{inhibitor}}/(D/k_1)_{\text{activator}} > 6$  (8, 16, 27–29).

The average ratio of the normalized diffusivities of Leftys and Nodals measured here is  $\mathcal{R} \approx 14$ , providing biophysical support for these modeling studies (see text S8 for comparison of reaction-diffusion systems). The different diffusivities in the Nodal/Lefty biological system have counterparts in chemical reaction-diffusion systems. For example, patterns can be generated in a starch-loaded gel by combining an activator (iodide) with an inhibitor (chlorite) in the presence of malonic acid (30). In this *in vitro* system, diffusion of the activator is hindered by binding to the starch matrix and is thought to result in a higher (factor of  $\sim 15$ ) diffusivity of the inhibitor. These models and our measurements raise the possibility that differential binding interactions and a ratio of at least a factor of 5 to 15 of inhibitor and activator diffusivities might be a general feature of reaction-diffusion-based patterning.

#### References and Notes

1. A. M. Turing, *Philos. Trans. R. Soc. London Ser. B* **237**, 37 (1952).
2. A. Gierer, H. Meinhardt, *Kybernetik* **12**, 30 (1972).
3. S. Kondo, T. Miura, *Science* **329**, 1616 (2010).
4. H. Meinhardt, *Cold Spring Harb. Perspect. Biol.* **1**, a001362 (2009).
5. H. Shiratori, H. Hamada, *Development* **133**, 2095 (2006).
6. Y. Chen, A. F. Schier, *Curr. Biol.* **12**, 2124 (2002).
7. D. E. Klein, V. M. Nappi, G. T. Reeves, S. Y. Shvartsman, M. A. Lemmon, *Nature* **430**, 1040 (2004).
8. S. Sick, S. Reinker, J. Timmer, T. Schlake, *Science* **314**, 1447 (2006).
9. D. Ben-Zvi, B. Z. Shilo, A. Fainsod, N. Barkai, *Nature* **453**, 1205 (2008).
10. A. D. Economou *et al.*, *Nat. Genet.* **44**, 348 (2012).
11. P. Müller, A. F. Schier, *Dev. Cell* **21**, 145 (2011).
12. A. Kicheva *et al.*, *Science* **315**, 521 (2007).
13. O. Wartlick *et al.*, *Science* **331**, 1154 (2011).
14. S. R. Yu *et al.*, *Nature* **461**, 533 (2009).

15. J. A. Le Good *et al.*, *Curr. Biol.* **15**, 31 (2005).
16. T. Nakamura *et al.*, *Dev. Cell* **11**, 495 (2006).
17. S. Zhou *et al.*, *Curr. Biol.* 10.1016/j.cub.2012.02.065 (2012).
18. K. W. Rogers, A. F. Schier, *Annu. Rev. Cell Dev. Biol.* **27**, 377 (2011).
19. A. F. Schier, *Cold Spring Harb. Perspect. Biol.* **1**, a003459 (2009).
20. V. Duboc, F. Lapraz, L. Besnardeau, T. Lepage, *Dev. Biol.* **320**, 49 (2008).
21. C. Grande, N. H. Patel, *Nature* **457**, 1007 (2009).
22. M. M. Shen, *Development* **134**, 1023 (2007).
23. Y. Chen, A. F. Schier, *Nature* **411**, 607 (2001).
24. L. Marjoram, C. Wright, *Development* **138**, 475 (2011).
25. L. Zhang *et al.*, *Biotechniques* **42**, 446, 448, 450 (2007).
26. T. Gregor, E. F. Wieschaus, A. P. McGregor, W. Bialek, D. W. Tank, *Cell* **130**, 141 (2007).
27. M. I. Granero, A. Porati, D. Zanacca, *J. Math. Biol.* **4**, 21 (1977).
28. S. Kondo, R. Asai, *Nature* **376**, 765 (1995).
29. M. Yamaguchi, E. Yoshimoto, S. Kondo, *Proc. Natl. Acad. Sci. U.S.A.* **104**, 4790 (2007).
30. I. Lengyel, I. R. Epstein, *Science* **251**, 650 (1991).

**Acknowledgments:** We thank X. Zhang for help with the cloning of Cyclops constructs, H. Othmer and A. Lander for helpful discussions, J. Dubrulle for discussions and primers for quantitative reverse transcription polymerase chain reaction, and S. Mango for comments on the manuscript. Supported by European Molecular Biology Organization and Human Frontier Science Program (HFSP) Long-Term Fellowships (P.M.), the NSF Graduate Research Fellowship Program (K.W.R.), NIH grant 5R01GM56211, and HFSP grant RGP0066/2004-C.

#### Supplementary Materials

www.sciencemag.org/cgi/content/full/science.1221920/DC1  
 Texts S1 to S8  
 Tables S1 to S8  
 Figs. S1 to S26  
 Movie S1  
 References (31–109)

14 March 2012; accepted 5 April 2012  
 Published online 12 April 2012;  
 10.1126/science.1221920

## Mechanical Control of Morphogenesis by Fat/Dachsous/Four-Jointed Planar Cell Polarity Pathway

Floris Bosveld,<sup>1\*</sup> Isabelle Bonnet,<sup>1\*</sup> Boris Guirao,<sup>1\*</sup> Sham Tlili,<sup>1†</sup> Zhimin Wang,<sup>1</sup> Ambre Petitalot,<sup>1</sup> Raphaël Marchand,<sup>1</sup> Pierre-Luc Bardet,<sup>1</sup> Philippe Marcq,<sup>2</sup> François Graner,<sup>1</sup> Yohanns Bellaïche<sup>1‡</sup>

During animal development, several planar cell polarity (PCP) pathways control tissue shape by coordinating collective cell behavior. Here, we characterize by means of multiscale imaging epithelium morphogenesis in the *Drosophila* dorsal thorax and show how the Fat/Dachsous/Four-jointed PCP pathway controls morphogenesis. We found that the proto-cadherin Dachsous is polarized within a domain of its tissue-wide expression gradient. Furthermore, Dachsous polarizes the myosin Dachs, which in turn promotes anisotropy of junction tension. By combining physical modeling with quantitative image analyses, we determined that this tension anisotropy defines the pattern of local tissue contraction that contributes to shaping the epithelium mainly via oriented cell rearrangements. Our results establish how tissue planar polarization coordinates the local changes of cell mechanical properties to control tissue morphogenesis.

**T**issue morphogenesis requires the coordination of cell behaviors during development. Planar cell polarity (PCP) pathways, which coordinate the polarization of cells in the

tissue plane, have been shown to play a fundamental role in morphogenesis of vertebrates and invertebrates (1). It remains largely unknown how PCP pathways control local cell mechan-

ical properties to drive global tissue deformation. The Fat/Dachsous(Ds)/Four-jointed(Fj) PCP pathway plays fundamental roles in the regulation of tissue growth, the orientation of cell polarity across the tissue, and the regulation of morphogenesis (1, 2). *fat* and *ds* encode proto-cadherins, whereas *fj* encodes a Golgi kinase modulating Fat/Ds binding (3–8). In many *Drosophila* tissues, *ds* and *fj* are expressed in tissue-wide opposing gradients (4, 5, 9, 10). Fat and Ds are reported to be homogeneous at the cell membrane (10, 11). Yet, the heterophilic binding of Fat and Ds between adjacent cells is proposed to generate

a tissue-wide polarity (7, 8, 10, 12–15). Through a poorly understood mechanism involving Fat signaling and the DHHC palmitoyltransferase Approximated (16), this polarity promotes the asymmetric distribution of the myosin Dachs, which controls division orientation and apical cell size (12, 16–19). The role of the Fat/Ds/Fj pathway in tissue morphogenesis has been studied by using indirect measurements such as the shape of clones and division orientation (19, 20); conversely, measurements of tissue dynamics have so far characterized its role in tissue rotation (21). Here, we assessed whether, where, and how the Fat/Ds/Fj pathway affects local cell mechanical properties to drive tissue deformations.

We implemented a multiscale imaging method to record morphogenesis of the *Drosophila* dorsal thorax during metamorphosis (22). This monolayered epithelium is composed of a posterior region, the scutellum, and of a large anterior region, the scutum (Fig. 1A and fig. S1, A and B). Cells were labeled with E-Cadherin: green fluorescent protein (GFP), and the tissue was imaged from 11 hours after pupa formation

(hAPF) to 36 hAPF by acquiring high-resolution three-dimensional stacks tiling the thorax at each time-point (Fig. 1A and movie S1). This multi-scale imaging enabled us to follow  $\sim 10^4$  cells over several cell cycles with unprecedented dynamics: 5 min resolution over 26 hours of development and  $0.32 \mu\text{m}$  resolution over the  $\sim 750 \times 700 \mu\text{m}^2$  of the tissue. At the cell-scale, the spatial and temporal resolutions facilitated the determination and the tracking of cell apex areas, cell shapes, divisions, cell rearrangements, and apoptoses (Fig. 1, B to D; fig. S1, C and D; and movie S2). At the tissue scale, we measured local tissue flow over the whole tissue by means of image correlation, using a length scale of 10 to 20 cells and a time scale of 2 hours. This revealed the different periods of development (fig. S2 and movie S3). In particular, between 17:20 and 21:20 hAPF the velocity map showed morphogenetic movements both in the scutum and the scutellum (Fig. 1E, shaded regions). This tissue flow promoted tissue contraction and elongation in the lateral scutum and the medial scutellum, resulting in their anterior-posterior and medial-

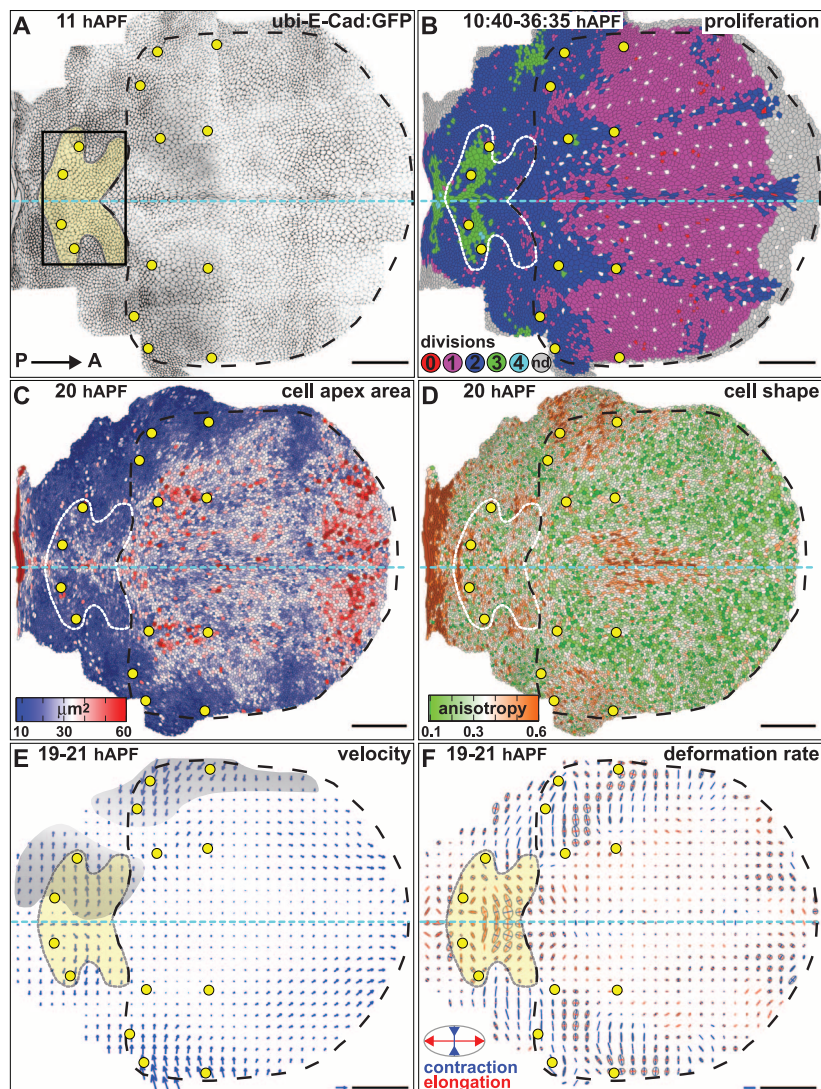
<sup>1</sup>Polarity, Division and Morphogenesis Team, Institut Curie, CNRS UMR 3215, INSERM U934, 26 Rue d'Ulm, 75248 Paris Cedex 05, France. <sup>2</sup>Laboratoire Physico-Chimie Curie, Institut Curie, CNRS UMR 168, Université Pierre et Marie Curie, 26 Rue d'Ulm, 75248 Paris Cedex 05, France.

\*These authors contributed equally to this work.

†Present address: Matière et Systèmes Complexes, Université Paris Diderot, CNRS UMR 7057, 10 Rue Alice Domon et Léonie Duquet, 75205 Paris Cedex 13, France.

‡To whom correspondence should be addressed. E-mail: johanns.bellaiche@curie.fr

**Fig. 1.** The *Drosophila* dorsal thorax as a system for morphogenesis. In all figures, yellow circles, macrochaetae; cyan dashed line, midline. **(A)** Dorsal thorax tissue labeled with E-Cad:GFP. Yellow region, scutellum; dashed black line, scutum. The black box cut by the midline defines the two “hemiscutella”. **(B to D)** Maps of proliferation (B), apex area (C), and anisotropy (D), defined as 1 minus the ratio of minor and major axes of the fitting ellipse. White cells are sensory organ precursor cells. **(E)** Velocity field averaged between 19 and 21 hAPF, represented as arrows. Gray regions are scutum and scutellum flows. **(F)** Deformation rates averaged between 19 and 21 hAPF, represented as ellipses. Red, elongation; Blue, contraction. Anterior (A). Posterior (P). Scale bars,  $100 \mu\text{m}$ ,  $9 \times 10^{-2} \mu\text{m}/\text{min}$  [(E), blue arrow],  $2.4 \times 10^{-3} \text{min}^{-1}$  [(F), blue bar].



lateral elongations, respectively (Fig. 1F, scutellum in yellow). Collectively, our multiscale imaging and measurements provide a resource to investigate how signaling pathways control tissue morphogenesis.

Looking for regulators of these morphogenetic movements, we observed that *ds* and *ff* were both expressed in the scutellum (fig. S3), their opposing gradients forming an inverted V-shaped domain pointing toward the midline (thereafter referred to as  $\Lambda$ -shape) in each hemi-scutellum (Fig. 2A and fig. S3). To understand the role of Fat/Ds/Fj signaling in tissue morphogenesis, we thus focused on the contraction and elongation taking place in the scutellum. The average tissue deformation rate map between 17:20 and 21:20 hAPF revealed that tissue deformation was not homogenous along the *ds* and *ff* gradients (Fig. 2B and fig. S4). This suggests that Fat/Ds/Fj activation might vary along the *ds* and *ff* gradients and emphasizes the need to define where the Fat/Ds/Fj pathway is active to investigate its role in morphogenesis. Given the evidence indicating that the subcellular localization of the myosin Dachs is controlled by Fat activity (17, 18, 23), we generated a Dachs:GFP (D:GFP) rescue construct and imaged it in the scutellum (movie S4). This revealed that (i) D:GFP was polarized in the  $\Lambda$ -shaped domain, where the opposing expression gradients of *ds* and *ff* meet (Fig. 2C); and (ii) within the regions of D:GFP planar polarization, cell boundaries enriched in D:GFP were aligned with each other, leading to D:GFP planar polarity lines (Fig. 2C, arrowheads).

Loss of *ds* or *fat* function as well as overexpression of *ff* disrupted D:GFP polarization (fig. S5, A to D). In agreement with the fact that D:GFP was mostly polarized in the region where the *ds* and *ff* gradients were opposed, clonal overexpression of either *ds* or *ff* induced repolarization of D:GFP only in regions where *ff* or *ds* were expressed, respectively (fig. S5, E and F). We then analyzed the subcellular localization of Fat, Ds, and Fj in relation with the Dachs polarization domain (fig. S6, A to C'') and established that Ds was polarized in regions where D:GFP was polarized (Fig. 2D and fig. S6, A to A''). Ds polarization required the *ff* gradient and Fat activity but was independent of Dachs activity (fig. S6, D to G'). Both Ds and D:GFP polarized toward high levels of *ff* expression and colocalized at the junctions (Fig. 3, A to C''). Furthermore, D:GFP can pull down the Flag:Ds intracellular domain (Fig. 3D). Altogether, our results revealed that Ds is planar polarized in the region where the opposing gradients of *ds* and *ff* meet. In turn, the interaction between Ds and Dachs promotes the polarization of Dachs (fig. S7, model).

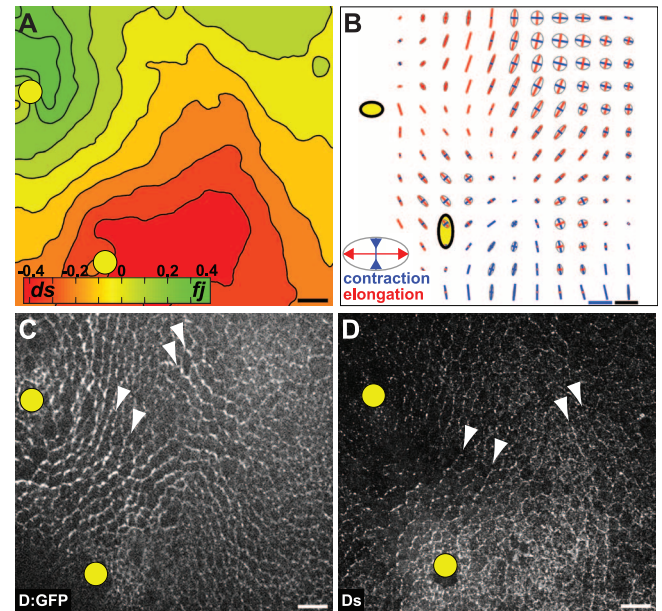
The ectopic accumulation of Dachs reduces cell apex area, suggesting its possible implication in mechanical apex constriction (19). To directly assess whether the Fat/Ds/Fj pathway modulates cell mechanical properties via Dachs polarization, we performed laser ablation of junc-

tions and observed that the tension of junctions enriched in D:GFP was on average twofold higher as compared with junctions devoid of D:GFP (Fig. 3E, fig. S8, and movie S5). To confirm that Dachs polarization leads to anisotropic junction tension, we generated *fat* clones that induced an increased polarization and an accumulation of Dachs in mutant junctions facing the wild-type ones (fig. S9, A and C). Such junctions displayed an increased tension that depends on Dachs activity (fig. S9B). Last, MyosinII was not polarized at the *fat* clone boundaries and did not exhibit a stronger anisotropy than the one due to cell shape itself, along the Dachs polarity lines (fig. S9, D to H). This shows that Dachs polarity regulates the anisotropy of junction tension and suggests that the opposing *ds* and *ff* gradients generate a tension anisotropy along Ds and Dachs polarity lines.

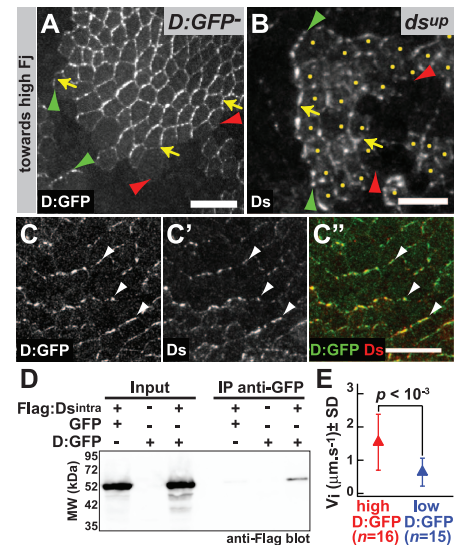
To investigate whether the tension anisotropy along the Dachs polarity lines control tissue morphogenesis, we developed a physical model that provides a general method to analyze the morphogenetic contribution of a specific signaling pathway within elaborate morphogenetic movements. In our case, it predicted that Dachs tension anisotropy is sufficient to modulate the local contraction rate (supplementary text). It provided a quantitative test to determine whether Dachs contributes to morphogenesis: Upon subtraction of the contraction rate of any mutant condition abrogating Dachs function or polarization from the contraction rate of the wild-type condition, the resulting difference in contraction rate is expected to be aligned with the Dachs polarity pattern.

To analyze the role of Dachs polarization, we first quantified the Dachs polarity pattern

**Fig. 2.** Ds and Fj expression gradients locally polarize Dachs and Ds. Panels show right-side hemi-scutellum. (A) Quantification of the average gradients of Ds and *ff-lacZ* ( $n = 7$  hemi-scutella). (B) Mean deformation rates ( $n = 5$  hemi-scutella) between 17:20 and 21:20 hAPF. Deformation rates represented as ellipses. Red, elongation; Blue, contraction. (C and D) Dachs:GFP (D:GFP) and Ds localization. Arrowheads: D:GFP (C) and Ds (D) polarity lines. Yellow ellipses indicate average macrochaete positions  $\pm$  SD. Scale bars, 10  $\mu\text{m}$ ,  $10^{-3} \text{ min}^{-1}$  [B, blue bar].



**Fig. 3.** Ds and Dachs colocalize and Dachs polarization is associated with tension anisotropy. (A and B) Cells located in a region of the Fj gradient expressing D:GFP and lacking D:GFP (*D:GFP<sup>-</sup>*) (A), or overexpressing *ds* (*ds<sup>UP</sup>* cells marked by mRFP, not shown) (B) accumulate D:GFP and Ds at junctions facing the higher Fj concentration (green arrowheads), whereas they are absent at junctions facing the lower Fj concentration (red arrowheads). Yellow arrows: direction of polarization. Yellow dots: *ds<sup>UP</sup>* cells abutting the wild-type (WT) cells (B). (C to C'') D:GFP [(C) and (C'')] and Ds [(C') and (C'')] colocalize (arrowheads). (D) Anti-Flag blot of GFP-immunoprecipitates from cells expressing Flag:Ds<sup>intra</sup> and GFP; Flag:Ds<sup>intra</sup>, Flag:Ds<sup>intra</sup> and D:GFP; Molecular weight (MW) markers in kilodaltons. Although a nonspecific GFP binding was observed, a larger amount of Flag:Ds<sup>intra</sup> was reproducibly coprecipitated with D:GFP. (E) Plot of the mean speed of vertex relaxation after ablation of junctions with high or low D:GFP. Scale bars: 10  $\mu\text{m}$ .



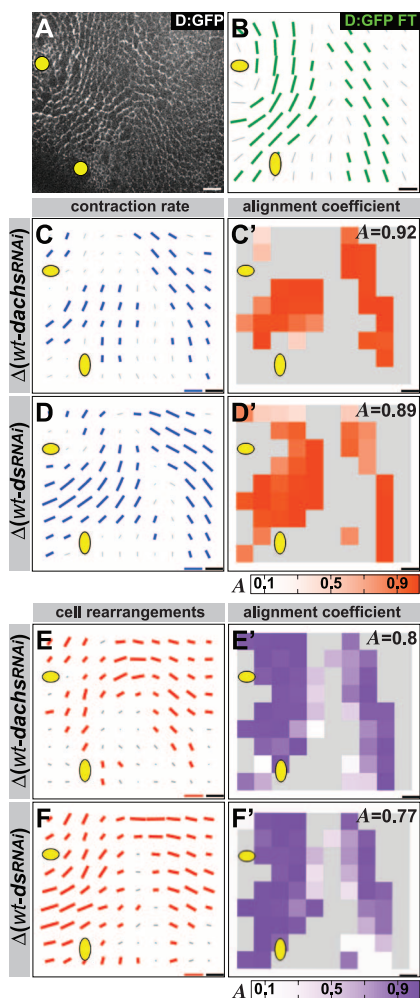


**Fig. 4.** Dachs polarity lines promote local contractions mainly via cell rearrangements. Averaged maps between 17:20 and 21:20 hAPF. **(A and B)** Localization of D:GFP **(A)** and map of D:GFP magnitude and anisotropy **(B)** quantified by Fourier Transform (FT,  $n = 3$  hemi-scutella). **(C to F')** Maps of subtractions of *dachs*<sup>RNAi</sup> ( $n = 5$  hemi-scutella) from WT ( $n = 11$  hemi-scutella) and of *ds*<sup>RNAi</sup> ( $n = 5$  hemi-scutella) from WT ( $n = 11$  hemi-scutella) for contraction rates [(C) and (D)] and for cell rearrangements [(E) and (F)]. Bars indicate amplitudes and orientations of the differences of contraction rates or cell rearrangements. Maps of the alignment coefficients between the D:GFP FT pattern and the differences in contraction rates [(C') and (D')], or between the differences in contraction rates and cell rearrangements within the D:GFP FT pattern [(E') and (F')] for WT and *dachs*<sup>RNAi</sup> [(C') and (E')] and for WT and *ds*<sup>RNAi</sup> [(D') and (F')]. Local alignment scores [(C') and (D'), orange; (E') and (F'), purple] go from 0 (fully anticorrelated), to 1 (fully correlated), through 0.5 (noncorrelated). Significant data are green **(B)**, blue [(C) and (D)], and red [(E) and (F)] bars; other are gray bars **(B)** to **(F)**. The average score *A* is calculated over nongray regions. Scale bars, 10  $\mu\text{m}$ ,  $5.5 \times 10^{-4} \text{ min}^{-1}$  [(C) and (D), blue bars],  $1 \mu\text{m}^2 \text{ min}^{-1}$  [(E) and (F), red bars].

(Fig. 4, A and B, green bars, and fig. S10). We then knocked down Dachs or Ds function by expressing *dachs* (*dachs*<sup>RNAi</sup>) or *ds* (*ds*<sup>RNAi</sup>) hairpins during pupal development and averaged between 17:20 and 21:20 hAPF the map of differences of the local contraction rates between wild-type and *dachs*<sup>RNAi</sup> or between wild-type and *ds*<sup>RNAi</sup> pupae. We observed significant differences in the local contraction rates between wild-type and *dachs*<sup>RNAi</sup> tissues or between wild-type and *ds*<sup>RNAi</sup> within the  $\Lambda$ -shaped domain of D:GFP polarization (Fig. 4, C and D, blue bars, and fig. S11, A to C). The orientations of the significant differences were aligned with the local orientations of the D:GFP anisotropy distribution (Fig. 4, C' and D'). These results demonstrate that Dachs polarization regulates tissue morphogenesis by increasing the rate of contraction along its polarity lines.

We then studied how Dachs polarization controls the cell dynamics that makes up the local tissue contractions. Our analyses of cell division rate and orientation argue against a major contribution of division orientation (fig. S12). We therefore quantified the respective contributions of cell rearrangements and cell shape changes to tissue contraction rates (fig. S13). In the wild-type tissue, Dachs polarization correlates with the cell rearrangement pattern both in magnitude and orientation (fig. S14, A to C', red bars), whereas it poorly correlates with cell shape changes (fig. S14, D and D', cyan bars). Accordingly, both the differences in tissue contraction rates between wild-type and *dachs*<sup>RNAi</sup> and between wild-type and *ds*<sup>RNAi</sup> were mainly associated with a decrease in the contribution of cell rearrangements to tissue contractions in the regions of Dachs polarization and, to a lesser extent, to cell shape changes ( $P < 10^{-12}$ ) (Fig. 4, E to F', and figs. S11, A' to C'', and fig. S15). Similar results for tissue contraction rate and cell dynamics were obtained in *fat*<sup>RNAi</sup> and *ff*<sup>UP</sup> mutant conditions (fig. S16). Accordingly, *ds*<sup>RNAi</sup>, *ff*<sup>UP</sup>, *fat*<sup>RNAi</sup>, and *dachs*<sup>RNAi</sup> pupae manifest similar defects in the adult scutellum shape (fig. S17).

Altogether, we found that Ds polarization promotes Dachs polarization within a domain of the opposing tissue-wide *ds* and *ff* gradients. Their local polarization produces an anisotropic distribution of junction tensions, which increases the contraction rates along the lines of Ds and Dachs planar polarization to shape the epithelial tissue mainly through oriented cell rearrangements (fig. S18). The Dachs myosin has the necessary domains to be an actin-binding motor (fig. S9) and, in complex with Dachsous, may directly contribute to junction contractility, favoring cell rearrangements. Because MyosinII also contributes to junction tension and cell rearrangements (24), future work should dissect the respective roles of Dachs and MyosinII in these processes. Morphogenesis is accomplished by the concerted activity of multiple signaling pathways. Our subtractive method of tissue deformation rates is general enough to isolate the contribution of a

given pathway to morphogenesis without making assumptions on its magnitude and its spatial dependence. Last, given the multitude of cell shapes, cell sizes, and division patterns occurring in the thorax epithelium, future work on this tissue should reveal how multiple signaling pathways are integrated to regulate proliferation, planar polarization, and morphogenesis.

**References and Notes**

1. L. V. Goodrich, D. Strutt, *Development* **138**, 1877 (2011).
2. F. A. Grusche, H. E. Richardson, K. F. Harvey, *Curr. Biol.* **20**, R574 (2010).
3. P. A. Mahoney *et al.*, *Cell* **67**, 853 (1991).
4. H. F. Clark *et al.*, *Genes Dev.* **9**, 1530 (1995).
5. M. H. Brodsky, H. Steller, *Dev. Biol.* **173**, 428 (1996).
6. H. O. Ishikawa, H. Takeuchi, R. S. Haltiwanger, K. D. Irvine, *Science* **321**, 401 (2008).
7. M. A. Simon, A. Xu, H. O. Ishikawa, K. D. Irvine, *Curr. Biol.* **20**, 811 (2010).
8. A. L. Brittle, A. Repiso, J. Casal, P. A. Lawrence, D. Strutt, *Curr. Biol.* **20**, 803 (2010).
9. C. H. Yang, J. D. Axelrod, M. A. Simon, *Cell* **108**, 675 (2002).
10. D. Ma, C. H. Yang, H. McNeill, M. A. Simon, J. D. Axelrod, *Nature* **421**, 543 (2003).
11. H. Strutt, D. Strutt, *Dev. Cell* **3**, 851 (2002).
12. E. Cho, K. D. Irvine, *Development* **131**, 4489 (2004).
13. H. Matakatsu, S. S. Blair, *Development* **131**, 3785 (2004).
14. J. Casal, P. A. Lawrence, G. Struhl, *Development* **133**, 4561 (2006).
15. H. Matakatsu, S. S. Blair, *Development* **133**, 2315 (2006).
16. H. Matakatsu, S. S. Blair, *Curr. Biol.* **18**, 1390 (2008).
17. Y. Mao *et al.*, *Development* **133**, 2539 (2006).
18. D. Rogulja, C. Rauskolb, K. D. Irvine, *Dev. Cell* **15**, 309 (2008).
19. Y. Mao *et al.*, *Genes Dev.* **25**, 131 (2011).
20. L. A. Baena-López, A. Baonza, A. García-Bellido, *Curr. Biol.* **15**, 1640 (2005).
21. B. Aigouy *et al.*, *Cell* **142**, 773 (2010).
22. Materials and methods are available as supplementary materials on Science Online.
23. G. Schwank *et al.*, *Dev. Cell* **20**, 123 (2011).
24. T. Lecuit, P. F. Lenne, E. Munro, *Annu. Rev. Cell Dev. Biol.* **27**, 157 (2010).

**Acknowledgments:** We thank J. Axelrod, S. Blair, Y. Hong, K. Irvine, E. Martin-Blanco, M. Simon, D. Strutt, S. Tsukita, the Bloomington Drosophila Stock Center, Transgenic RNAi Project, and Vienna Drosophila RNAi Center for reagents; M. Coppey, A. Houdusse, F. Molino, S. Ritzenthaler, F. Serman, J. Shi, and the PICT-IBISA@BDD for help; V. Hakim, E. Heard, J. Lopez-Gay, M. Labouesse, and A.-M. Lennon for comments. This work was supported by ARC-4830, L'Agence Nationale de la Recherche–MorphoDro, and European Research Council–CePoDro grants; a Fondation pour la Recherche Médicale grant to I.B.; and a Nederlandse Organisatie voor Wetenschappelijk Onderzoek–Rubicon grant to F.B.

**Supplementary Materials**

www.sciencemag.org/cgi/content/full/science.1221071/DC1  
 Materials and Methods  
 Supplementary Text  
 Figs. S1 to S20  
 References  
 Movies S1 to S5

27 February 2012; accepted 30 March 2012  
 Published online 12 April 2012;  
 10.1126/science.1221071